Journal of the European Ceramic Society 45 (2025) 117570

Contents lists available at ScienceDirect

Journal of the European Ceramic Society

journal homepage: www.elsevier.com/locate/jeurceramsoc

Influence of powder characteristics on the rheology of ceria-based screen-printing pastes for solid oxide cell applications

Denise J. Ramler [a,b,*], Robert Mücke [a], Christian Lenser [a], Olivier Guillon [a,b,c], Norbert H. Menzler [a,b]

[a] Institute of Energy Materials and Devices (IMD), Materials Synthesis and Processing (IMD-2), Forschungszentrum Jülich GmbH, Jülich 52425, Germany
[b] Institute of Mineral Engineering (GHI), RWTH Aachen University, Aachen 52074, Germany
[c] Jülich Aachen Research Alliance – Energy (JARA), Jülich 52425, Germany

ARTICLE INFO

Keywords:
Rheology
Solid oxide cells
Screen-printing
Particle size distribution
Gadolinium-doped ceria

ABSTRACT

Screen-printing is a widely utilized method for fabricating solid oxide electrolysis cells (SOECs), a promising technology for efficient hydrogen production. This study focuses on the rheological characterization of screen-printing pastes, emphasizing the influence of ceramic powder properties on rheological behavior and layer features. Conventional metrics such as viscosity, or binder and ceramic content provided in wt% are shown to inadequately describe paste characteristics. Instead, we propose the use of dynamic rheological properties, including damping factor and yield point, and introduce a bimodality coefficient φ to be able to quantify and correlate particle size distribution shapes with these rheological properties. Results demonstrate that dry layer thickness and dimensional accuracy correlate strongly with the damping factor, revealing that pastes with higher damping factors exhibit thinner layers due to increased viscous behavior. Additionally, increasing the amount of binder in relation to the specific surface area (SSA) of the ceramic particles weakens the 3-dimensional paste network, decreasing yield points and shifting paste behavior toward predominantly viscous behavior. Analysis of SSA as well as particle size distribution (PSD) and their correlation with rheology highlights the destabilizing effect of agglomerates in asymmetrical and bimodal particle size distributions, underscoring the need for comprehensive powder characterization.

1. Introduction

Solid oxide cells (SOCs) have the potential to become an important technology for the global transition toward sustainable energy systems [1]. In electrolysis mode (SOEC), these cells efficiently produce hydrogen as an energy carrier or a basic feedstock for the chemical industry. In reverse operation, fuel cell mode (SOFC), the produced hydrogen (or carbohydrates like methane) is converted into electricity. This means that producing power or chemicals is possible within the same system or cell structure. This functionality is only possible if the individual components or layers of such SOCs exhibit distinct microstructures. Fuel and air electrodes must have a porous microstructure so that the relevant gases can access the reaction sites at the electrolyte interface, while the electrolyte between those electrodes must provide a dense microstructure to keep the reaction gases separated. In fuel electrode-supported cells, the support, the functional electrode and the electrolyte are co-sintered, meaning both porous and dense layers must be produced simultaneously. To this day, the fabrication of these cells relies predominantly on suspension-based processes, such as screen-printing and tape casting, due to their simplicity and adaptability [2–4]. Despite their widespread utilization, these methods demand continuous improvements to enhance the quality and reproducibility of deposited layers, particularly in terms of thickness uniformity and microstructure optimization. Among the various materials explored for SOCs, gadolinium-doped ceria (GDC) is recognized as a state-of-the-art electrolyte and electrode material due to its favorable ionic and mixed ionic-electronic conductivity [5], [6–8]. However, its incorporation into fuel electrode-supported solid oxide cells (FESOCs) has yet to be fully established. The main challenge in the production of such GDC-based cells is the interdiffusion that can occur during sintering between GDC and yttria stabilized zirconia (YSZ) containing layers, as it leads to the formation of porosity at the electrochemically active interface between

* Corresponding author at: Institute of Energy Materials and Devices (IMD), Materials Synthesis and Processing (IMD-2), Forschungszentrum Jülich GmbH, Jülich 52425, Germany.
E-mail address: d.ramler@fz-juelich.de (D.J. Ramler).

https://doi.org/10.1016/j.jeurceramsoc.2025.117570
Received 28 February 2025; Received in revised form 27 May 2025; Accepted 28 May 2025
Available online 29 May 2025

fuel electrode and electrolyte [9]. Furthermore, the mixed phase increases the ohmic resistance of the electrolyte, negatively impacting cell performance [10]. One approach to mitigate this interdiffusion is to reduce the sintering temperature. However, ensuring sufficient densification and subsequent gas tightness of the electrolyte while lowering the sintering temperature is challenging. A potential solution is to increase the available ceramic surface area to boost sintering activity. As a logical consequence, the paste formulations need to be adjusted accordingly in order to continue to ensure their processability. In general, rheological characterization offers valuable knowledge of the properties required for advancing the screen-printing process [11]. However, current understanding of how paste composition influences the rheological behavior remains incomplete. Therefore, investigating and understanding how rheological characteristics can be adjusted is key to addressing these challenges, as it could provide critical insights into the fabrication process. While significant attention has been directed toward the roles of solid [12–15] REF and binder content [14,16–19] , less emphasis has been placed on the contribution of intrinsic properties of the ceramic particles used in these pastes. This gap in knowledge hinders the ability of researchers to replicate experimental results and often leads to inconsistencies when applying findings across different studies. For example, discrepancies arise when trying to compare results from different publications that consider the binder content in pastes. This is not least due to the complexity of the topic and the number of possible variations in the paste formulations and commercially available products. For example, Ried et al. present viscosities of different YSZ electrolyte pastes at shear rates of 100 s^{-1} [14]. Here, two pastes show different viscosities with 6 Pa•s and 10 Pa•s despite the same solids content (50 vol%) and the same binder content and binder type (PVB Mowital B30H, 0.25 wt%). Although the apparent reason for this is the use of YSZ powders from different manufacturers, the exact difference between the powders causing the deviation in viscosity is not analyzed. Moreover, their work concludes that in general pastes with viscosities (at 100 s^{-1}) in the range of 4 Pa•s to 12 Pa•s are suitable for screen printing, but one of the two above-mentioned pastes (η = 10 Pa•s) is declared as not printable. This inevitably raises the question of whether viscosities are a sufficient means of evaluating screen printing pastes, and whether weight percentage data for the binder provide sufficient information about the general composition of the pastes, and if not, what other information is needed. This is additionally supported by findings of Somalu et al., who report that NiO/ scandia stabilized zirconia (ScSZ) pastes with viscosities within this given range are perceived as unsuitable for screen printing [20]. The reason provided for this discrepancy is the different paste composition without further explanation. Similar inconsistencies also arise when comparing the NiO/ScSZ pastes of Somalu et al. [21] with $La_{0.6}Sr_{0.4}Ti_{0.3}Fe_{0.7}O_{3-\delta}$ (LSTF) pastes of Murakami et al. [19]. In both studies, the pastes contained 20 vol% (70 wt%) of the respective ceramic component and 1 wt% ethyl cellulose as a binder, homogenized in terpineol. However, the viscosities at 100 s^{-1} also differ greatly here, with approximately 15 Pa•s for the NiO/ScSZ paste and < 1 Pa•s for the LSTF paste. Again, the cause for these differences can be found in the use of different powders. However, since the influence of the powder is not given much attention, it is hardly possible to adapt test results from the literature to one's own research. Especially for scientists who are trying to transfer new materials into already known systems, this lack of understanding results in massive difficulties. In some cases, studies that claim to have used different powder preparation methods combined with varying binder contents, the rheological data is presented in an inadequate and thus unusable fashion. For example, in the work by Zhang et al. on YSZ electrolyte pastes, only viscosities are given as a function of solids content, without information on shear rate, powder type or binder content [22].

This approach limits the ability to discern how variations in powder characteristics, such as particle size distribution and specific surface area, affect rheological behavior and, consequently, the quality of printed layers. Addressing this limitation could improve understanding and reproducibility in such suspension-based manufacturing processes. Therefore, this work aims to demonstrate that the conventional presentation of rheological data – such as reporting viscosities as function of binder or ceramic content solely in weight or volume percent – fails to convey meaningful insights into paste composition and component interactions. Therefore, we demonstrate that expressing binder content relative to the ceramic surface area provides a clearer and more comparative framework for evaluating rheological properties. In addition, dynamic rheological properties such as damping factor, storage and loss modulus are used to characterize the pastes and their yielding behavior. This allows for a more detailed description of the viscoelasticity of pastes than is possible with flow curves and viscosity data. Furthermore, it is shown that the description of the ceramic powder with traditional d_{10}, d_{50} and d_{90} values (diameters of the particles that are 10 %, 50 % and 90 % of the particles in the distribution) is insufficient. The shape of the particle size distribution, on the other hand, is presented to show clear correlations with the relevant rheological properties. For this purpose, a method is presented for quantifying the shape of a distribution using a bimodality coefficient φ and thus making such data usable.

2. Methodology

2.1. Rheology of screen-printing pastes

The viscosity η is the most widely known rheological property [23]. Screen printing pastes show a reduction in viscosity with increasing shear rates, which is generally referred to as shear-thinning behavior or pseudoplasticity. Viscosities are often used to assess the quality of a suspension by means of flow or viscosity curves. For example, irregularities in the curve may indicate agglomeration of particles in the suspension. It is also possible to use the viscosity to quantify and evaluate the degree of particle dispersion in fixed systems. In most cases, a lower viscosity at low shear rates indicates a better dispersion. However, previous studies have already shown that viscosity alone is not sufficient to adequately describe the behavior and quality of pastes for the printing process. Instead, it was discovered that the viscoelastic properties of pastes have a much more significant influence on the printing result [11].

Screen-printing pastes as viscoelastic materials exhibit both viscous (liquid-like) and elastic (solid-like) behavior [24]. Viscoelasticity is a dynamic property and therefore best analyzed using oscillatory rheometry. In oscillation amplitude sweep tests, a sample is excited sinusoidally, resulting in a sinusoidal strain γ (deformation) or stress τ response. This response can then be divided into an elastic and viscous component individually, thus providing access to the quantitative determination of the elastic and viscous properties of the material. Energy that is stored within the sample upon excitation is represented by the storage modulus G' and corresponds to elastic behavior. On the other hand, energy that dissipates is expressed within the loss modulus G'', which describes viscous behavior [25]. Pastes have a load range in which this viscoelasticity is independent of stress or strain. Within this range, structural changes are almost completely reversible. Therefore, this area is referred to as the linear viscoelastic region (LVR). The ratio of loss modulus G'' to storage modulus G' within the LVR provides information about the general behavior of a paste and is defined as the damping factor tan δ according to Eq. 1. This factor indicates whether the material behaves dominantly viscous (tan δ > 1) or dominantly elastic (tan δ < 1).

$$tan\delta = \frac{G''}{G'} \tag{1}$$

Furthermore, the end of the LVR is defined as the yield point (γ_y strain-based yield point, τ_y stress-based yield point). Beyond this point, deformation is associated with an irreversible or only partially reversible change in the paste's structure. In general, the yield point is a metric for

the strength of this three-dimensional ceramic-binder network. Studies have already shown that this network strength is largely dependent on the solid- and binder content of a paste. In principle, as solids or binder content increase, the yield point is shifted to higher shear stresses or strains, indicating larger network strengths. However, the ratio of these two components also influences network strength, so that it appears to weaken again if extreme ratios are exceeded. Additionally, the value of the yield point is also sensitive to the method of analysis. Experiments with controlled shear stresses often lead to less frequency-dependent yield points than strain-based experiments. Nevertheless, the latter are preferred in practice. The reason for this is that the change in structural strength depends directly on the deformation, whereas shear stress only indirectly influences the extent of the deformation. Furthermore, there exist several calculation methods for the yield point. For this work, the offset method was applied for the calculation using amplitude sweep results. Here, the point at which the measurement curve deviates from a tangent of the *G'* curve in the LVR by 3 % was determined as the yield point, as visualized in Fig. 1.

Additionally, materials that initially exhibit dominant elastic behavior within the LVR, possess the ability to transition into dominant viscous behavior or flow. The point at which the transition occurs is defined as the flow point (γ_f strain-based flow point, τ_f stress-based flow point). It is the cross-over point of storage and loss modulus ($G' = G''$) in an amplitude sweep test. The area between yield point and flow point can be described as the yield range. As suggested and reported on in more detail by Wei et al., the transition behavior can be quantified with the Flow Transition Index (FTI) according to Eq. 2 [26]. *FTI* values close to 1 would indicate abrupt yielding of a brittle material, whereas *FTI* $>>$ 1 is describing a more flexible material and gradual yielding.

$$FTI = \frac{\gamma_f}{\gamma_y} \quad , regarding\ strain. \qquad (2)$$

$$FTI = \frac{\tau_f}{\tau_y} \quad , regarding\ stress.$$

Since strain responses show a certain dependence on the frequency used during the amplitude sweep, it is advisable to also calculate *FTI* values using shear stresses, even if the difference is found to be minimal [27].

Another crucial property of screen-printing pastes is thixotropy. It is characterized by a time-dependent decrease of flow resistance when a constant shear stress is applied, followed by a gradual recovery if that load is removed. During the screen-printing process, the paste must flow easily under the mechanical forces of the squeegee to fill the mesh and transfer onto the substrate. After the transfer, the paste should regain its structure again in a feasible timeframe to prevent unwanted effects, such as slumping or bleeding. If the recovery is too rapid, it can hinder the leveling of the paste, leading to uneven surfaces or incomplete filling of the mesh openings, which may lead to visible mesh-imprints in the printed layer. The appropriate time for structural rebuilding depends mainly on the printing parameters and the screen used. Factors such as the speed of separation (substrate from screen) and the thread thickness of the mesh play a key role. In general, thixotropy and yielding behavior are closely linked through their relationship with the internal network structure of a material and its response to applied stress.

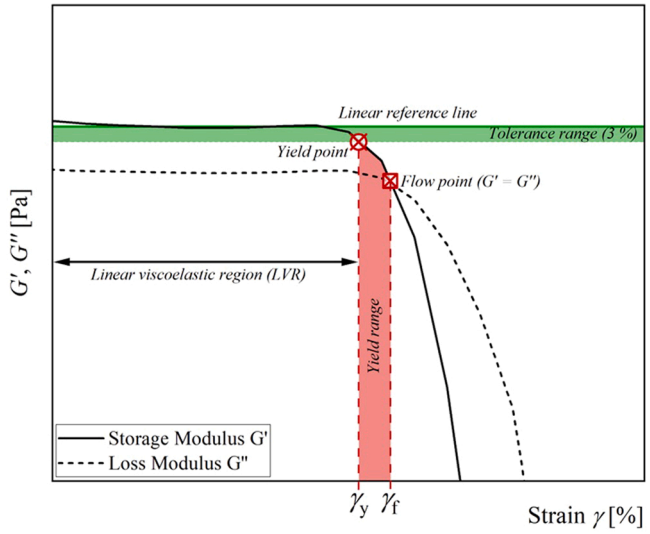

Fig. 1. G' and G'' of a paste during a strain-based oscillatory amplitude sweep test. Yield point γ_y determination via offset method, flow point γ_f, linear viscoelastic region (LVR) and yield range are indicated.

2.2. Bimodality coefficient

The characterization of ceramic powders typically focuses on two key properties: particle size distribution (PSD) and specific surface area (SSA). Only the d_{10}, d_{50} and d_{90} values are usually provided to describe the PSD. These values represent the particle diameters at the 10th, 50th and 90th percentile of the distribution fall below, respectively. However, while these metrics are useful for summarizing the range of particle sizes, they offer limited insight into the overall shape of the distribution. This lack of detail poses challenges when trying to investigate and quantify the influence of the PSD on the rheological properties of ceramic pastes. Therefore, in this work, Sarle's bimodality coefficient φ was calculated for each powder, providing a different approach to quantifying particle size distribution shapes [28]. This coefficient considers both skewness and excess kurtosis of a given distribution. The exact calculation method for this bimodality coefficient is detailed in the supporting information.

Values for the bimodality coefficient range between 0 and 1, whereby a monomodal distribution can be assumed up to a value of approx. 0.55. Values above 0.55 indicate a bimodal distribution. As visualized in Fig. 2, positive values for skewness indicate a right-skewed (or left-leaning distribution), which would likely occur with powders that were milled from larger particle sizes as the case in this work (top-down processing). Similarly, positive values for excess kurtosis indicate narrow distributions with long tails to both sides, whereas negative values hint toward broad distributions with short tails.

3. Experimental

3.1. Paste preparation

A commercially available $Gd_{0.1}Ce_{0.9}O_{1.95}$ starting powder (GDC10-M, Fuelcellmaterials, USA) was characterized for its particle size distribution (PSD) by static laser scattering method (SLS, using a LA-950V2, HORIBA Europe GmbH, Germany), specific surface area (SSA) by nitrogen gas adsorption (Area Meter II, Juwe Laborgeräte GmbH, Germany) and particle morphology via scanning electron microscopy (SEM, Zeiss GeminiSEM 450, Carl Zeiss Microscopy Deutschland GmbH, Germany). With an as-delivered SSA of 39 m^2/g, this powder is considered too fine for highly concentrated dispersions [29,30]. Therefore, various pre-treatment steps were carried out to adjust its properties. To increase the primary particle size and to reduce the SSA, powder batches were pre-calcined at 1130 °C, 1230 °C and 1340 °C for 3 h each and subsequently milled to obtain powders with primary grain sizes and d_{50} values of about 0.1 µm ± 0.03 µm. Two different approaches for milling were used that resulted in bimodal or monomodal particle size distributions. Bimodal distributions were prepared by low-energy ball milling using tumbling mixers (PE-bottles, 48 h, 72 rpm in EtOH with 3 – 5 mm YSZ grinding balls, Turbula T2F, Willy A. Bachofen AG, Switzerland). High-energy milling in a planetary ball mill (YSZ lined steel container, 15 cycles of 5 min milling + 25 min pause, 500 rpm in EtOH with <

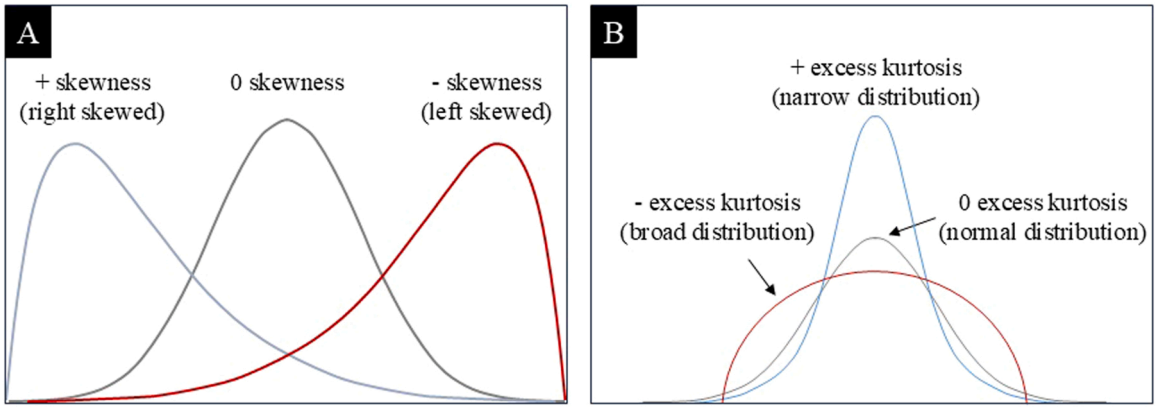

Fig. 2. Schematic illustration of positive and negative skewness compared to a normal distribution (A) and positive and negative excess kurtosis compared to a normal distribution (B).

1 mm YSZ grinding balls, Pulverisette 7 premium line, FRITSCH GmbH, Germany) was used to achieve monomodal particle size distributions. However, monomodal distributions with narrow peaks at the target grain size of 0.1 μm could not always be achieved with this method. In some cases, distributions with long tails to higher particle sizes or even with small but clearly defined peaks at particle sizes between 1 μm to 10 μm were obtained. Nevertheless, these powders were still used to be able to correlate rheological properties of pastes with a larger number of varying particle size distributions. After these pre-treatment procedures, the powders were characterized again for their particle size distribution, morphology and specific surface area.

All pastes contained α-terpineol ($C_{10}H_{18}O$, Sigma-Aldrich Chemie GmbH, Germany) as solvent, Hypermer KD2 (Croda International Plc, United Kingdom) as dispersant and ethyl cellulose as the binder component, whereby a medium-length ethyl cellulose (viscosity of 45 mPa•s of a reference solution) was used. The mixing of components always followed the same methodology. First, the dispersant was dissolved in α-terpineol. Then, the GDC powder was dispersed in this α-terpineol dispersant solution, using an ultrasonic bath. Finally, a transport suspension consisting of α-terpineol, and ethyl cellulose was added to this pre-suspension. After pre-mixing by hand, final paste homogenization was achieved by a three-roll mill (Exakt 80 E, EXAKT Advanced Technologies GmbH, Germany) utilizing the settings displayed in Table 1.

With this, various pastes with different compositions (solids and binder content) were produced, whereby only the ratios of these components were varied but not their type. Only the type of GDC powder differs from paste to paste in most cases due to different particle size distributions and specific surface areas. For each paste, a dispersant concentration of 13 mg/m² in reference to the SSA of the powder was used.

3.2. Rheological measurements

All rheological measurements were carried out using the modular compound rheometer Physica MCR 301 (Anton Paar Germany GmbH, Germany). The data was collected using serrated parallel plates with a plate diameter of 25 mm. This configuration was chosen to minimize wall-slip effects. The plate spacing was set to 0.5 mm. Each measurement was performed at 20 °C and maintained via a temperature control unit (Julabo F25-EH, JULABO GmbH, Germany). A pre-shearing step at a shear rate of 1 s^{-1} for 60 s was done for every measurement, which was followed by a resting period ($\dot{\gamma} = 0\ s^{-1}$ for 60 s). This is to nullify stresses within the internal structure of the paste that may occur as a result of placing and compressing the sample in the shear gap.

For this work, amplitude sweep tests were conducted in a strain range of 0.1 – 1000 % with a logarithmic increase of 6 points per decade and an angular frequency ω of 10 rad/s. Strain γ, shear stress τ, temperature T, storage G' and loss modulus G'' as well as the phase angle δ were recorded during the measurement. To further characterize the viscoelastic behavior of pastes, yield and flow point were calculated from the amplitude sweep measurement using the RheoCompass software (Anton Paar Germany GmbH, Germany).

For pastes that showed a transition into flow, the 3-interval-thixotropy test (3ITT) was carried out to evaluate their thixotropic behavior and to gain more information about the recovery of the internal structure after the printing process. During the first interval, the sample is loaded with very low shear stresses to simulate conditions at rest. For this, values from within the linear viscoelastic range are taken that were established in the amplitude sweep test. Rest conditions are set to be at a strain amplitude of 1 % applied with an angular frequency ω of 10 rad/s, which was held constant for 60 s. In the second interval, the paste is subjected to very high shear in rotational mode. This is to simulate the coating process, altering the internal structure of the sample. Shear rates of above 1000 s^{-1} commonly occur during screen-printing but are highly dependent on the printing setup and the screen mesh [31]. For our process, shear rates of roughly 3000 s^{-1} were calculated and used for the measurement. These were applied for 5 s, similar to the duration of the printing process. In the third interval, the same load settings as in the first interval are applied to again simulate a state at rest conditions after the coating process. In this way, a quasi-undisturbed rebuilding of the structure can be analyzed. A summary of the measurement parameters for each interval are shown in Table 2.

Table 1
Parameters for paste homogenization using a three-roller mill. Pastes are subjected to each setting for at least three passes.

#	1. Gap [μm]	2. Gap [μm]	Line pressure [N/mm]	Speed [rpm]
1	60	20	-	90
2	30	10	-	90
3	10	5	-	90
4	5	-	1.5	70

Table 2
Measurement parameters for each interval of the 3-intervall-thixotropy test (3ITT). Intervals I and III were measured in oscillation mode and interval II in rotational mode.

Interval	I	II	III
Angular frequency ω	10 rad/s	-	10 rad/s
Strain γ	1 %	-	1 %
Shear rate $\dot{\gamma}$	-	3000 s^{-1}	-
Meas. pt. duration	5.0 s	0.5 s	5.0 s
Interval duration	59 s	5 s	386 s
Temperature T	20 °C	20 °C	20 °C

3.3. Layer printing and evaluation criteria

All coatings evaluated in this work were printed on polished 50 mm× 50 mm x 1.5 mm stainless steel substrates using an EKRA E2 semi-automatic screen printer (EKRA Automatisierungssysteme GmbH, Germany). The squeegee pressure was kept constant at 1.5 bar (0.15 MPa), squeegee speed at 110 mm/s and the snap-off distance at 1.6 mm. A polyester screen with a screen opening of 40 mm× 40 mm and a mesh with 48 threads/cm and a thread thickness of 55 μm was used for printing. As the layers were not printed in an air-conditioned laboratory, yet temperature and humidity have an influence on the rheological properties of pastes, care was taken to print the layers on days under similar conditions. After printing, all layers were dried at 60 °C for a minimum of 24 h.

Analogous to the work of Mücke et al., the dried layers were scanned with the optical inspection system CT300T (cyberTECHNOLOGIES GmbH, Germany) using a DRS-500 triangulation laser sensor (125 nm vertical resolution with a spot size of 16–23 μm) [13]. A differential scanning method was used to obtain information about the height and area of the printed layers. For this, after the initial scanning, the substrates were cleaned, dried and scanned again. The measurement data of the blank substrates was then subtracted from their corresponding layer measurement to acquire the differential data set of the isolated layer. With this, potential sources of errors like substrate unevenness or scratches could be circumvented. For each paste, a minimum of three samples were printed and measured.

In this work, the print quality is evaluated by the geometric accuracy of the print image and the thickness of the dried layer d_{dry}. A fidelity factor F_{PE} is introduced for quantifying the dimensional accuracy. According to Eq. 3, it is calculated from the ratio of the edge length of the screen opening X_S to the edge length of the print image X_P. The higher the value, the closer the dimensional accuracy (also see Fig. 3). For a screen opening of 40 mm× 40 mm, values for F_{PE} are always expected to be close to 100 %. This is because effects like paste bleeding become more pronounced when using screens with smaller openings.

$$F_{PE} = \frac{X_S}{X_P} \times 100 \quad (3)$$

4. Results and discussion

4.1. Powder properties

Calcination of the starting powder with subsequent grinding resulted in the desired increase in primary grain size. Fig. 4 compares a scanning electron micrograph of the starting powder with one of the powders calcined at 1230 °C and ground in the tumbling mixer. On average, the initial primary particle size of 0.07 μm was coarsened to approx. 0.1 – 0.2 μm by the pre-treatments. At the same time, the results of the nitrogen adsorption show that the specific surface area was reduced from the original 39 m^2/g to 7 m^2/g for this powder and values between 6 m^2/g and 16 m^2/g for the others, depending on pre-calcination temperature and grinding method.

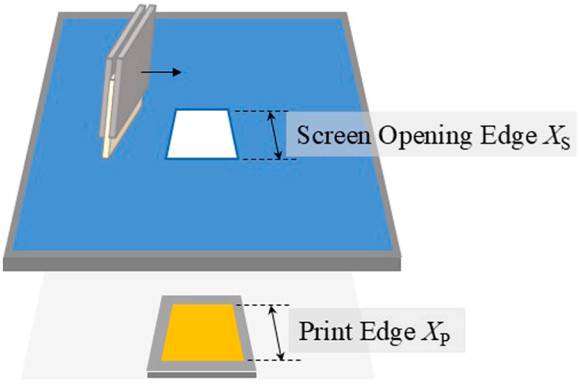

Fig. 3. Graphical representation of the parameters for calculating the fidelity factor. Screen with screen opening at the top and a substrate with a printed image below.

However, in order to better understand the influence of the particle size distribution on subsequent rheological properties, further quantification was needed. For example, two comparable particle size distributions in Fig. 5 show very similar d_{10}, d_{50} and d_{90} values but significantly different distribution shapes. This difference is reflected in the calculated bimodality coefficient. The distribution in A, which appears bimodal with a long tail towards larger grain sizes, therefore also shows a higher bimodality coefficient than the monomodal distribution in B.

4.2. Influence of rheological properties on printed layers

In this work, layers of five different pastes were evaluated based on dry layer thickness d_{dry} and geometric accuracy F_{PE}, with Table 3 presenting the solids and binder content of these pastes, their rheological parameters damping factor tan δ and yield point γ_y and the results of the evaluation criteria. Rheological properties such as viscosity, storage and loss modulus are not listed, as there appeared to be no statistical significance when correlating these values to the evaluation parameters using regression lines. Plots for these parameters are provided in the supporting information (see supporting information Fig. S1 – S3). Therefore, the following focuses solely on the yield point and the damping factor. If only the solids and binder content is considered, the lowest solid content of paste P4 also seems to result in the thinnest layer thickness of 50 μm. However, this correlation is not entirely clear when comparing pastes P2 and P3, which achieve layer thicknesses with a difference of approximately 10 μm while having the same apparent composition. Additionally, the resulting layer thickness of paste P3 is very similar to that of paste P4 while having 8 wt% more solids.

A clearer correlation can be found when analyzing the damping factor and yield point. In Fig. 6, the damping factor is plotted against the measured dry layer thickness and fidelity factor. The corresponding R^2 and Pearson r values are given in Table 4 for the regression lines. With $R^2 > 0.9$ in each case, both fits show a high degree of conformity with the data. In addition, a Pearson r value > 0.9 indicates a strong linear correlation between the damping factor and the resulting dry layer thickness, as well as the fidelity factor. When considering the layer thickness, a higher value for the damping factor seems to lead to thinner dried layers. This can be explained by the increasing proportion of viscous behavior as the damping factor increases. If the proportion of viscous behavior increases, simultaneously the proportion of elastic solid behavior decreases, and the paste becomes more capable of flowing. This increase in flowability then can lead either to a denser packing of the ceramic particles or to a bleeding of the paste, both of which could result in a reduction of the layer thickness. When comparing these results with the influence on the fidelity factor, a similar trend is observable. Paste P5 with the lowest damping factor results in layers with the highest dimensional accuracy. However, paste P4 does not show the lowest fidelity, although it resulted in the lowest layer thickness. This would indicate that a denser packing with less bleeding effect is achievable with this paste. Another possible explanation for this is that in pastes with higher damping factors, potentially a reduced quantity of paste is filled into the screen meshes during initial flooding of the screen, shortly before the actual printing process. The amount of paste that can be filled into each individual mesh is determined by adhesion and surface tension effects. A lower damping factor could potentially result in the formation of more pronounced concave menisci, effectively reducing the volume of paste within the mesh opening. This in turn would lead to less material being transferred onto the substrate, subsequently resulting in thinner layer thicknesses.

Though, it must be noted that the correlation of the data with the

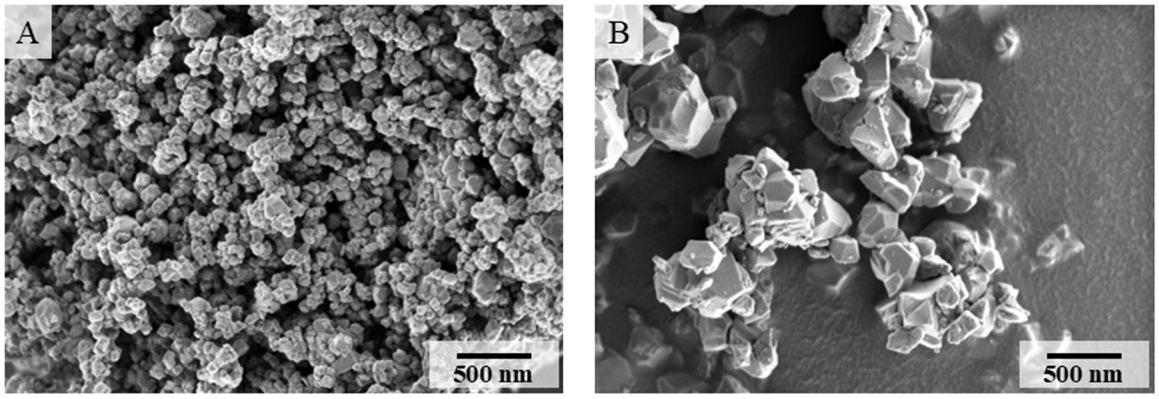

Fig. 4. Scanning electron micrographs taken with an InLens detector. A: Commercially available starting powder GDC10-M with a primary grain size of approx. 0.07 µm. B: Powder calcined at 1230 °C and subsequently milled in a tumbling mixer resulting in a primary grain size of approx. 0.1–0.2 µm combined to larger agglomerates.

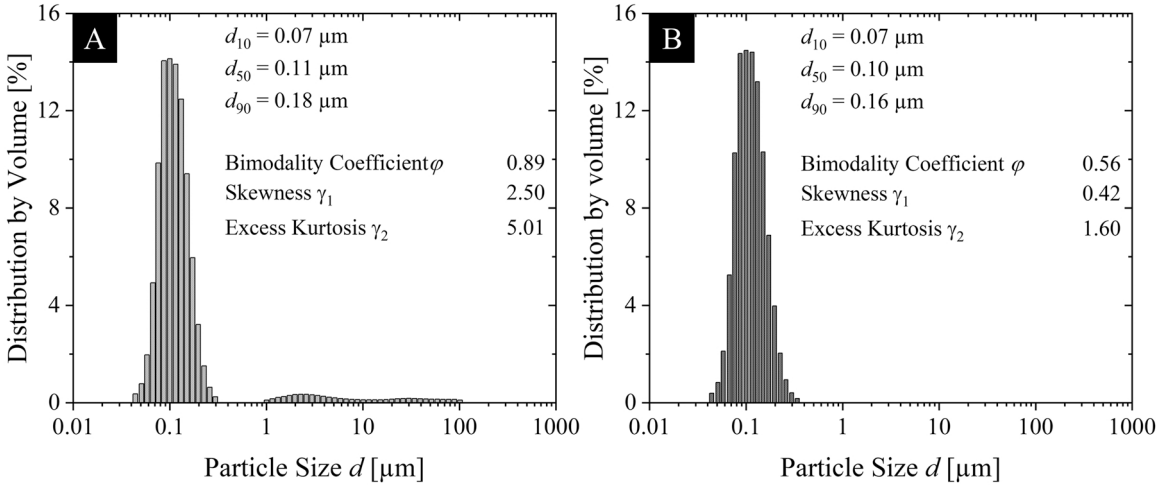

Fig. 5. Comparison of two particle size distributions. Although d_{10}, d_{50} and d_{90} values are very similar, both distributions show different shapes, which can be further quantified using distribution determinants such as the bimodality coefficient φ, skewness and kurtosis. Distribution A with a φ of 0.89 shows a quantified bimodality, while distribution B with a φ of 0.56 shows a quantified monomodality. Both powders were prepared in a planetary ball mill using the same settings.

Table 3
Solids and binder content of 5 different pastes and their rheological parameters loss factor, yield point and flow point if applicable. Indication of an average layer thickness and an average dimensional accuracy of printed and dried layers. Layers were produced under identical conditions.

#	Solids [wt. %]	Binder [wt. %]	Grain Size $d_{10}/d_{50}/d_{90}$ [µm]	Damping Factor tan δ [1]	Yield Point γ_y [%]	Flow Point γ_f [%]	Layer Thickness d_{dry} [µm]	Fidelity Factor F_{PE} [%]
P1	68	2	0.07 / 0.10 / 0.17^P	0.79	58	87	70 ± 2	99.8 ± 0.0
P2	64	3	0.07 / 0.10 / 0.16^P	0.97	52	58	62 ± 3	99.5 ± 0.0
P3	64	3	0.07 / 0.12 / 0.24^T	1.1	43	-	51 ± 1	99.1 ± 0.1
P4	56	5	0.12 / 0.20 / 0.32^T	1.14	42	-	50 ± 2	99.2 ± 0.0
P5	63	3	0.07 / 0.10 / 0.17^P	0.93	52	53	63 ± 2	99.4 ± 0.0

P: Planetary Ball Mill
T: Tumble Mixer

regression line for the fidelity factor is slightly lower and that the data, even if marginal, is subject to a certain error. Nevertheless, a higher loss factor seems to lead to a lower dimensional accuracy of the printed image.

When correlating the yield point with the dry layer thickness and the fidelity factor in Fig. 7 A and B, it appears that yielding occurring at higher deformations leads to higher layer thicknesses and dimensional accuracy. This can be explained by a higher particle-binder network strength indicated by a higher yield point. A higher network strength implies that the forces between particles and binder molecules are stronger at rest and the structure is more resistant to plastic deformation [32]. This network strength is partially restored after the printing process.

Additionally, if it is already greater at rest conditions, the network strength is potentially not reduced as much by the printing process compared to pastes with lower yield points. The less pronounced plastic deformation of pastes with higher yield points would then lead to higher layer thicknesses as indicated by the data.

When looking more closely at the transition behavior of the pastes that showed both a yield and a flow point, expressed as the *FTI*, the more

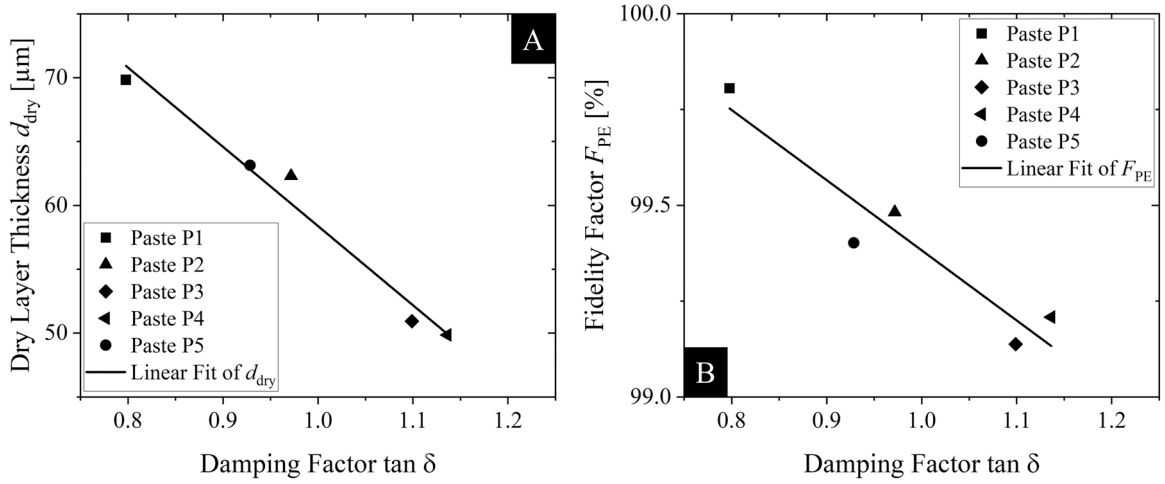

Fig. 6. Depiction of the influence of the damping factor tan δ on the dry layer thickness d_{dry} ($R^2 = 0.97$) (A) and on the fidelity factor F_{PE} ($R^2 = 0.90$) (B) with regression lines using 5 different pastes. Damping factors were obtained of the linear range during the amplitude sweep test.

Table 4
R^2 and Pearson r values for the regression lines of damping factor tan δ and yield point γ_Y in relation to the dry layer thickness d_{dry}. The regression was fitted using 5 different pastes in each case.

	Dry Layer Thickness d_{dry}		Fidelity Factor F_{PE}	
	R^2	Pearson r	R^2	Pearson r
Damping Factor tan δ	0.97	−0.99	0.90	−0.95
Yield Point γ_Y	0.99	0.99	0.93	0.96

flexible paste that showed a gradual transition into flowing ($FTI >> 1$) resulted generally in both higher dry layer thickness (see Fig. 8 A) and higher fidelity factor (see Fig. 8 B).

This can be explained by the thixotropic behavior, which was analyzed in the 3ITT. When comparing the results of the 3ITT from Fig. 9 with the transition behavior, it becomes clear that the transition behavior acts opposite to the thixotropic behavior. Flexible pastes that transition into flow over a longer deformation range appear to regain part of their original structure much more quickly after the printing process. For example, paste P1 shows the most flexible transition behavior, but regains its elastic-dominant behavior just 5 s after the printing process. In comparison, Paste P5 exhibits the shortest transition range and is not able to recover to elastic-dominant behavior in the given measurement period of 386 s. In terms of dry layer thickness and fidelity, this means that the faster a paste regains elastic-dominant behavior, the higher the layer thickness and fidelity, as they also lose their mobility more quickly after the printing process and become rigid again.

4.3. Influence of the ceramic powder

In principle, it is more straightforward to correlate rheological properties with parameters such as layer thickness or fidelity, as these rheological properties comprise complex interactions of several factors into one quantifiable value. To then analyze and evaluate the effects of individual components on these interactions is much more challenging. Nevertheless, an attempt was made to analyze the influence of various paste components of the given system on the resulting rheological paste properties. Analogous to Table 3, information about the additional 4 pastes can be found in Table S1 in the supporting information. Typically, only the d_{50} value of the powder is given when reporting on rheological behavior of pastes or layer manufacturing in general. If this value is correlated with the damping factor and yield point, as shown in Fig. 10A and B respectively, no clear trend emerges. This would indicate that in this case, the median particle size itself has no distinguishable influence on these rheological properties. Furthermore, when correlating the amount of solid content with either damping factor or yield point, there

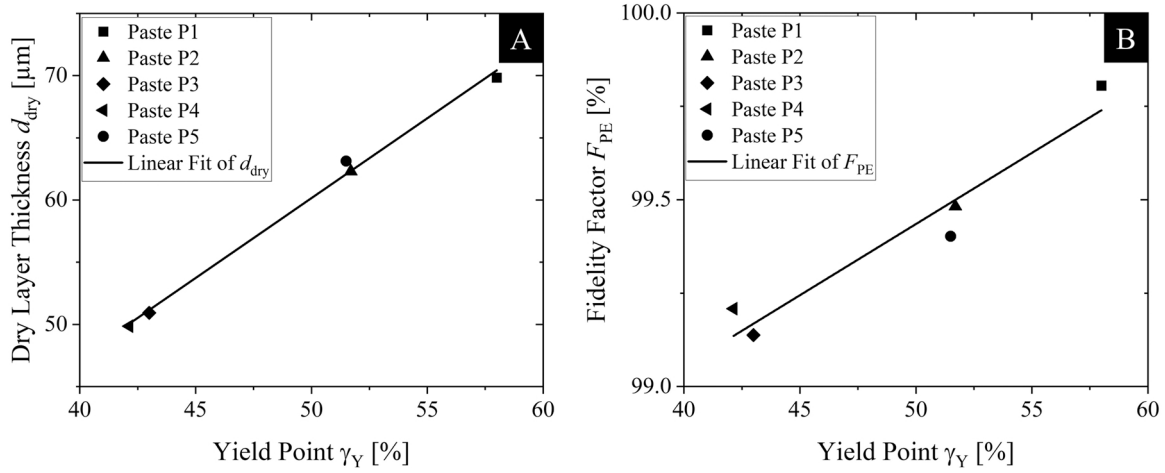

Fig. 7. Depiction of the influence of the yield point γ_Y on the dry layer thickness d_{dry} ($R^2 = 0.99$) (A) and on the fidelity factor F_{PE} ($R^2 = 0.93$) (B) with regression lines using 5 different pastes. Yield points were obtained at the end of the linear range during the amplitude sweep test.

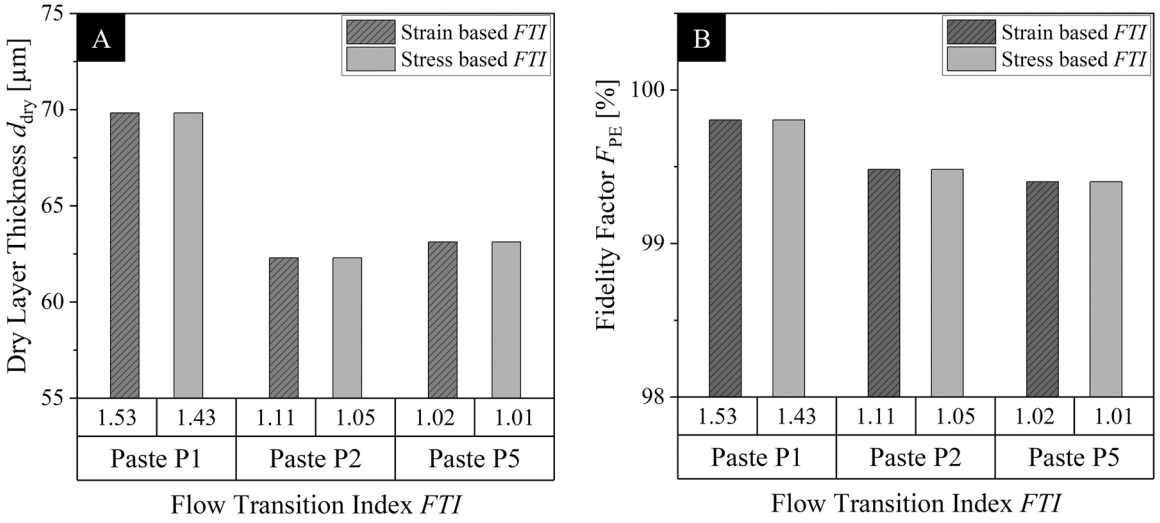

Fig. 8. Strain-based FTI and stress-based FTI vs dry layer thickness d_{dry} (A) and fidelity factor F_{PE} of 3 tested pastes, that had both a yield and a flow point and showed a transition behavior into flowing. Values for yield and flow point were obtained during the amplitude sweep test.

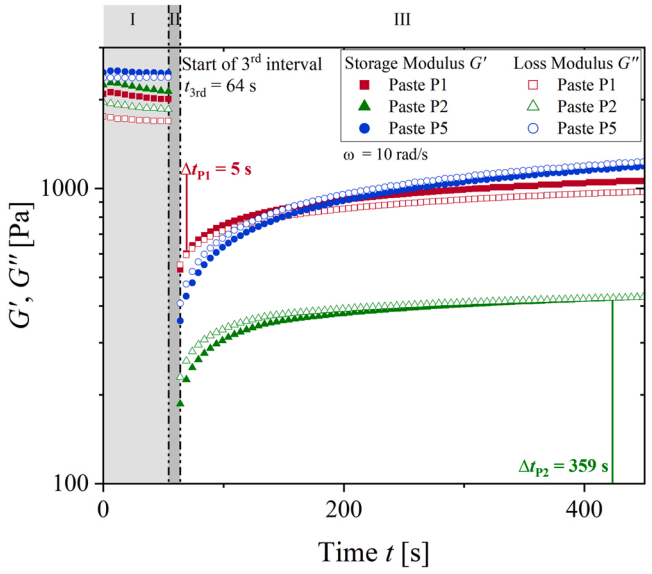

Fig. 9. Results of the 3ITT for Paste P1 (red), Paste P2 (green) and Paste P5 (blue). Recording of the measured values in the first and third interval using oscillation. Simulation of the printing process in the second interval using rotation (no measured values for storage and loss modulus). Vertical lines and Δt indicate the time within the 3rd interval where structural recovery ($G'' = G'$) occurs. Measured at 20 °C with a serrated plate-plate system (25 mm).

is also no trend observable within the tested range, as depicted in Fig. 10C and D.

However, if the powder and its PSD are analyzed in more detail using the previously mentioned parameters bimodality coefficient, skewness and kurtosis, clear linear correlations between the powder and damping factor emerge, as shown in Fig. 11 A - C with R^2 values being 0.75, 0.87 and 0.89 respectively. Compared to the correlation of rheological properties with, for example, layer thickness, the R^2 values here are lower. As already described previously, this is due to the fact that only one aspect is considered here, but rheological properties result from the interaction of several factors. This effect can be clearly seen in pastes or data points that lie directly above each other in these graphs. In these cases, multiple pastes with different compositions, were produced from the same powder, also resulting in slightly different rheological properties although the trend stays the same. However, the shape of the particle size distribution or agglomeration does not appear to have a significant influence on the yield point, as displayed in Fig. 11 D-F.

These results show that as the asymmetry of the particle size distribution increases, the damping factor also increases, which results in the viscous behavior of the paste becoming more pronounced or even dominating. The asymmetry of the particle size distribution is most likely stemming from residual agglomerates or re-agglomeration. To illustrate this effect, Fig. 12 shows amplitude sweeps of three pastes with the same composition using powders with different PSDs. The green and blue curves show amplitude sweep results of pastes made from monomodal powder ($\varphi = 0.53$ and $\varphi = 0.55$ respectively) and the red curves show the results of a paste made from bimodal powder ($\varphi = 0.82$). All three pastes contain the same solid content of 64 wt% and binder content of 3 wt%. The only difference between these pastes is the particle size distribution of the GDC powder used. Here the influence of the PSD on the damping factor becomes clear, as the pastes with monomodal distributions have dominating elastic behavior in the linear region ($G' > G''$), whereas the paste with the bimodal distribution exhibits dominating viscous behavior ($G' < G''$).

This is an indication that the typically forming three-dimensional network gets destabilized by agglomerates that are in this case 10–100 times larger than the average particle. This destabilization then would lead to the paste behaving more like a suspension with untangled polymer chains and viscous material behavior dominates. These relationships are also reflected when looking at the specific surface area of the powders. Here again there appears to be a linear relationship between specific surface area and damping factor, so that the damping factor increases as the surface area is minimized (Fig. 13 A). In this study, a smaller surface area is the result of incomplete break-up of the agglomerates during the grinding process. Therefore, with the same powder treatment, the surface area can already provide indications of possible residual agglomerates and subsequent paste behavior. Consequently, analogous to the particle size distribution, the specific surface area also shows no meaningful linear correlation with the yield point (Fig. 13 B).

4.4. Influence of the polymer binder

When evaluating the influence of the binder content, especially when comparing pastes made with different powders, it is more useful to consider the ratio of binder content to ceramic surface area rather than weight ratios. With this approach, the relationship between the polymer chain and its ceramic anchor point to form a three-dimensional network

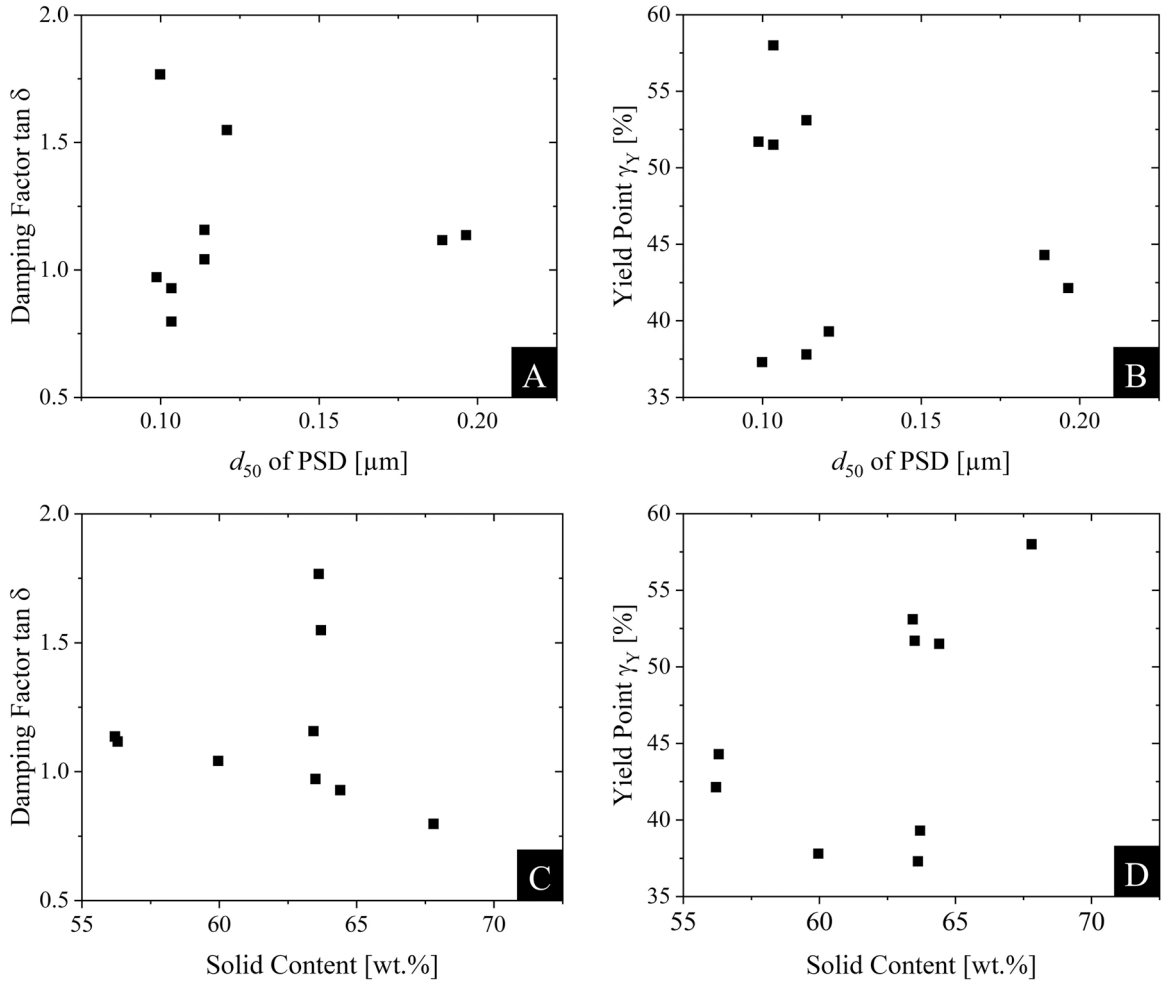

Fig. 10. d_{50} of PSD vs damping factor tan δ (A) and yield point γ_y (B). Solid content in wt% vs damping factor tan δ (C) and yield point γ_y (D) of 9 different pastes. None of these show any correlation.

is taken into account. This allows for a more straightforward analysis of the rheological data. Fig. 14 A shows the influence of the binder content per ceramic surface area on the damping factor. Although a regression line is displayed here, the fit with an R^2 value of 0.39 only poorly matches the data. Accordingly, a significant correlation cannot be definitively established. Nevertheless, the weak correlation would indicate that the damping factor increases with increasing binder content per ceramic surface area.

A further indication of this correlation can be found in the direct comparison between two pastes with similar particle size distributions, but different binder content as displayed in Fig. 14 B. Here, the paste with the lower binder content displays elastic-dominant behavior in the linear region ($G' > G''$), whereas the paste with the higher binder content exhibits viscous-dominant behavior ($G' < G''$). It seems as if by exceeding a certain binder content, there are not enough particles available as linking points and as if the paste is rather approaching the behavior of the binder suspension, which acts as an uncross-linked polymer melt [33].

For the yield point, however, there is a clear correlation with the binder per ceramic surface area with the R^2 of the fit being 0.81 (Fig. 15 A). Here it is indicated that with an increase in binder per ceramic surface area, the yield point shifts to lower deformations, implying that the network strength decreases with an increasing binder content. This relationship is even more pronounced when comparing two pastes made from the same powder but with different binder contents, as shown in Fig. 15 B. Displayed here in green, the paste with the lower binder content only yields at higher deformations, which indicates a higher network flexibility. However, the yielding behavior is also different. Initially, both the storage and loss modulus increase, which is hypothesized to indicate microcracks forming within the structure, that only completely penetrate the measuring gap at higher deformations, characterized by the kinking of the curves after passing through their respective maximum [25]. Interestingly, while the paste with the lower binder content starts to yield at higher strains, its critical yield stress (2300 Pa) is lower when compared to the paste with the higher binder content (2600 Pa). This apparent discrepancy highlights the differences between deformation and mechanical resistance when attempting to evaluate yielding behavior of complex fluids. Here, a higher critical strain indicates that pastes with a lower binder content per ceramic surface area can undergo larger deformation before their structure breaks down, suggesting a more flexible network structure. However, the paste simultaneously yielding at lower stresses implies that its internal structure shows less resistance to an applied force. Conversely, the paste with the higher binder content yields at a lower strain but higher

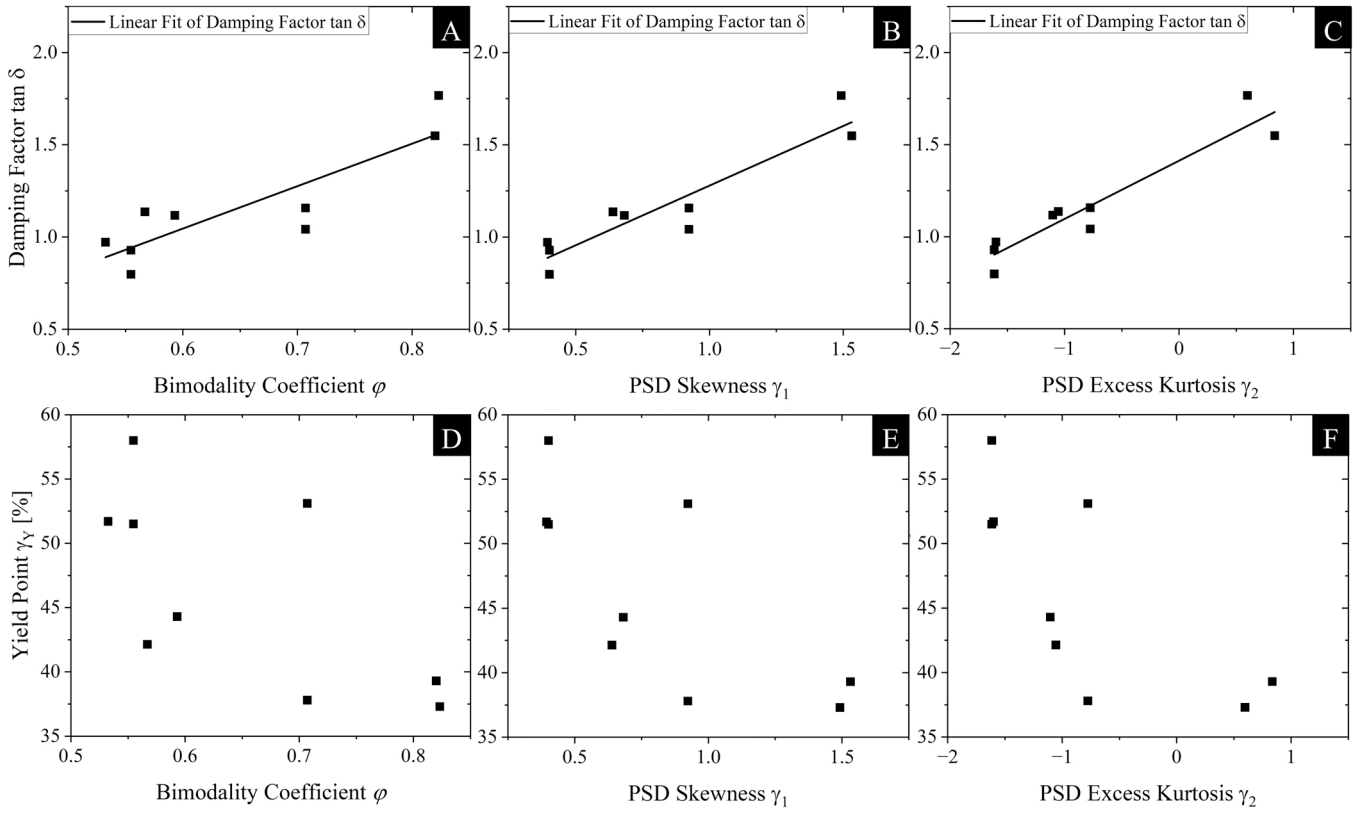

Fig. 11. Damping factor tan δ vs. powder characteristics bimodality coefficient φ ($R^2 = 0.75$), skewness γ_1 ($R^2 = 0.87$) and excess kurtosis γ_2 ($R^2 = 0.89$) (A-C) with a linear fit. Yield point γ_Y vs. powder characteristics bimodality coefficient, skewness and excess kurtosis (D-F) without a linear fit. Values of the rheological parameters were obtained from the amplitude sweep test.

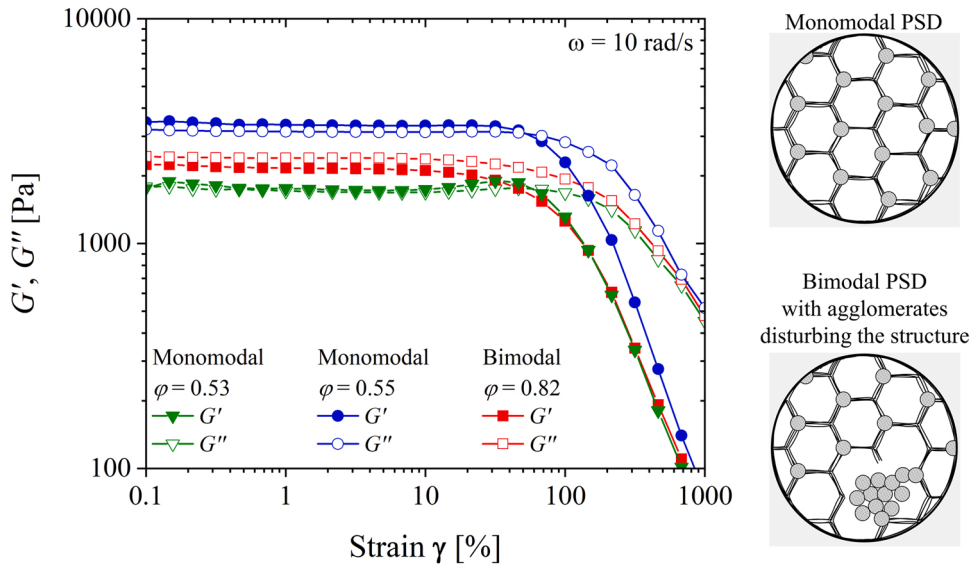

Fig. 12. Results of amplitude sweep tests for pastes with monomodal powder (green and blue) and a paste with a similar composition but bimodal powder (red). Measured at 20 °C with a serrated plate-plate system (25 mm) and an angular frequency of 10 rad/s. All three pastes contained 64 wt% of ceramic particles and 3 wt % of binder.

stress, which is indicative of a stiffer, more brittle network that is not able to deform as extensively before failure. While both critical stress and strain provide valuable insight, we argue that the latter is the more practically relevant parameter in the context of screen printing. This is due to the fact that screen printing involves substantial, rapid deformations, causing the pastes to exceed their respective linear viscoelastic range. Furthermore, the stresses applied during printing typically far surpass the critical yield stresses of these pastes. Therefore, the extent of deformation the network structure can tolerate before yielding offers more direct information about print fidelity and the structure rebuilding and integrity during and after the printing process, as already demonstrated in this work.

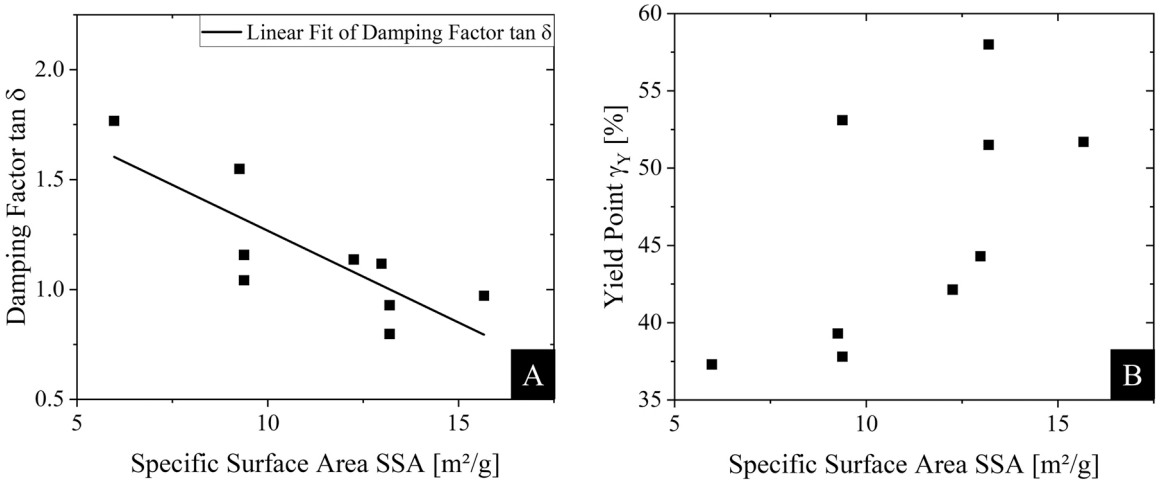

Fig. 13. Specific surface area SSA vs. damping factor tan δ (A) with a linear fit ($R^2 = 0.66$). Specific surface area SSA vs. yield point γ_y without a linear fit (B). Values of the rheological parameters were obtained from the amplitude sweep test.

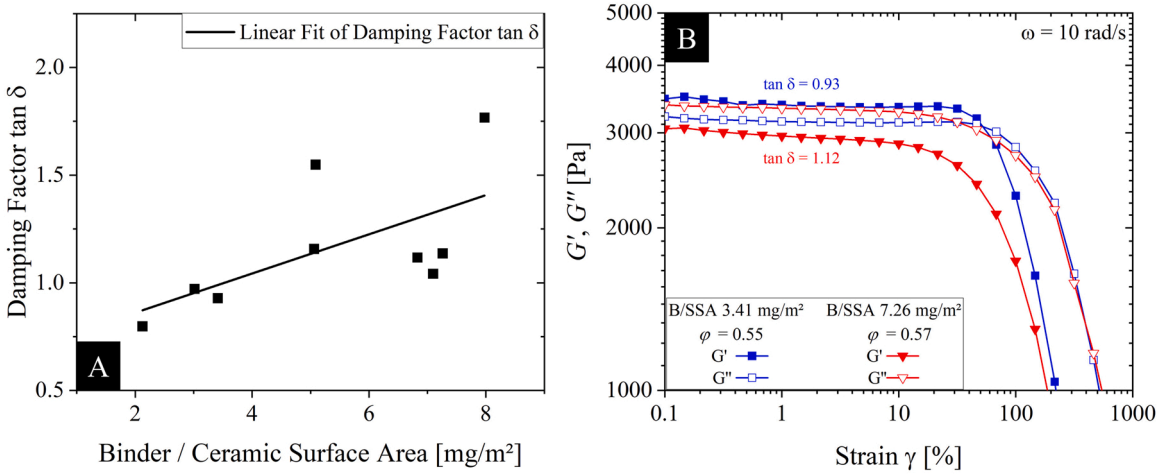

Fig. 14. Binder content per ceramic surface area vs. damping factor tan δ (A) with a linear fit ($R^2 = 0.39$) Results of amplitude sweep tests for two pastes with monomodal powder and low binder content (blue) and significantly higher binder content (red) (B). Measured at 20 °C with a serrated plate-plate system (25 mm) and an angular frequency of 10 rad/s.

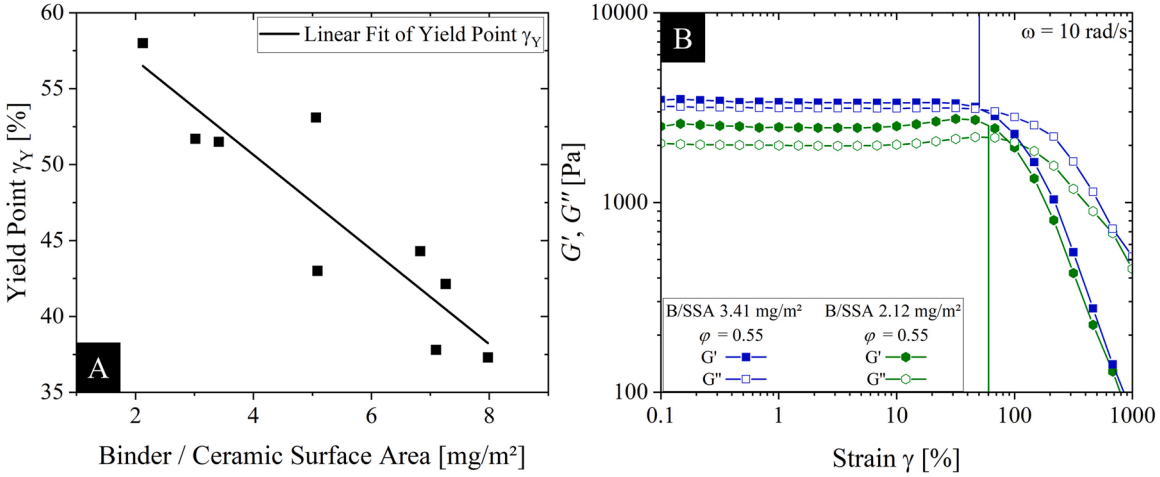

Fig. 15. Binder content per ceramic surface area vs. yield point γ_y with a linear fit ($R^2 = 0.81$) (A). Results of amplitude sweep tests for pastes made from the same powder and a higher binder content per ceramic surface area (blue) and a lower binder content per ceramic surface area (green) (B). Here, vertical lines indicate the position of the respective yield points. Measured at 20 °C with a serrated plate-plate system (25 mm) and an angular frequency of 10 rad/s.

4.5. Practical case studies: impact of rheology on GDC electrolyte layer printing

The layers quantitatively evaluated in this work were printed on dense metal substrates and not on actual, partially inhomogeneous and porous fuel electrode substrates. Since layer formation is also partially influenced by the substrate, it can be assumed that layers printed on metal substrates might differ from layers printed on unpolished ceramic substrates. Therefore, some examples of how rheology impacts printed GDC layers on real fuel electrode substrates will be presented here.

For example, pastes exhibiting issues such as bleeding can behave differently on porous compared to dense substrates. The capillary forces of the substrate surface may cause these pastes to partially penetrate into the support. As a result, defects in the underlying layers are not covered up but instead are transferred to the newly applied layer. To showcase this effect, Fig. 16 shows two SEM images of SOC half-cells with GDC electrolyte on NiO-GDC fuel electrode and NiO-YSZ substrates.

The electrolyte shown in Fig. 16 A was printed with a paste that had a damping factor tan $\delta >> 1$ which resulted in an average layer thickness of 2.3 ± 0.5 µm after sintering. The paste used for the electrolyte in Fig. 16 B had a damping factor tan $\delta < 1$. It can be seen that the layer in image B is significantly more uniform and better defined with greater layer thickness of 10.3 ± 0.2 µm, although both layers were printed and sintered identically and only showed differences in paste formulation and resulting rheological behavior.

Another common issue are screen imprints. Fig. 17 shows laser microscope images of two different GDC electrolyte surfaces. The electrolyte surface in Fig. 17 A clearly shows repetitive and deep screen marks. In contrast, the electrolyte surface in Fig. 17 B is free of such defects. The difference between the two GDC pastes used can be found in the height of the yield point. The mesh imprints probably result from using a paste that is too stiff and does not yield enough during the pressing process.

The paste used in A only begins to yield at a deformation of almost 60 %, while the paste in B already shows structural changes at a deformation of 43 %. These differences in yielding are due to the different binder-to-ceramic surface area ratios within the pastes, which was higher for the paste that exhibited screen imprints. However, it should be noted that screen imprints can also occur if an improper screen is used. The probability of screen imprints occurring decreases with a reduction in the thread thickness. Additionally, the thread material can affect the mesh intersection points. In general, it is recommended to use screens with a metal mesh rather than polyester screens for very high-resolution and fine structures.

Another phenomenon that can occur in the production of screen-printed layers are drying cracks. During this study, pastes with very fast recovery times in the 3ITT ($t < 10$ s) in particular exhibited cracks after drying at 60 °C (see Fig. 18). A reduction in the drying temperature had no influence on the formation of cracks. We propose that this is likely due to the internal structure already rebuilding very fast during the initial phase of drying, probably forming strong bonds between particles, binder and solvent. When the solvent evaporates, it presumably pulls on the already rigid binder and ceramic network, which in turn would result in high forces, leading to the formation of drying cracks. However, to gain a clearer understanding of the mechanisms at play, rheological characterizations at drying temperatures of 60 °C should be carried out in future investigations.

5. Conclusion

This study highlights the influence of rheological properties on the dried layer thickness and geometric accuracy in screen-printing processes and how these properties are influenced by paste composition. Among the properties analyzed, damping factor and yield point demonstrated significant impacts, with the damping factor negatively correlating with layer thickness and geometric accuracy, and the yield point exhibiting the opposite trend. Conversely, viscosity, values for loss and storage modulus showed no notable correlations. These findings emphasize the importance of understanding and controlling paste rheology to optimize printing outcomes.

While solid content showed no detectable influence on damping factor or yielding behavior within the tested range, further investigation into the paste components revealed that particle size distribution asymmetry significantly affects the damping factor, likely due to agglomerates disrupting the 3D network structure within the paste. Traditional powder characterization metrics, such as d_{10}, d_{50}, and d_{90} values, were found insufficient in capturing relationships between rheological behavior and the powder. Instead, a bimodality coefficient, derived from skewness and excess kurtosis, provided a more meaningful characterization. Additionally, binder content analysis revealed that weight percentage alone is inadequate for predicting rheological behavior. Instead, assessing binder content relative to the ceramic particle surface area yielded more robust correlations, particularly with the yield point. Here it was found that excessive binder content weakened the network structure, as indicated by shifts in the yield point to lower deformation values. These findings emphasize the importance of precise powder characterization in understanding and predicting paste rheology. This paper provides valuable insights and starting points for optimizing paste formulations, potentially enabling the assessment of paste rheology at the powder characterization stage. Such advancements could lead to improved efficiency and accuracy in screen-printing applications. However, it is essential to acknowledge that these findings represent only an initial exploration of the complex relationships and

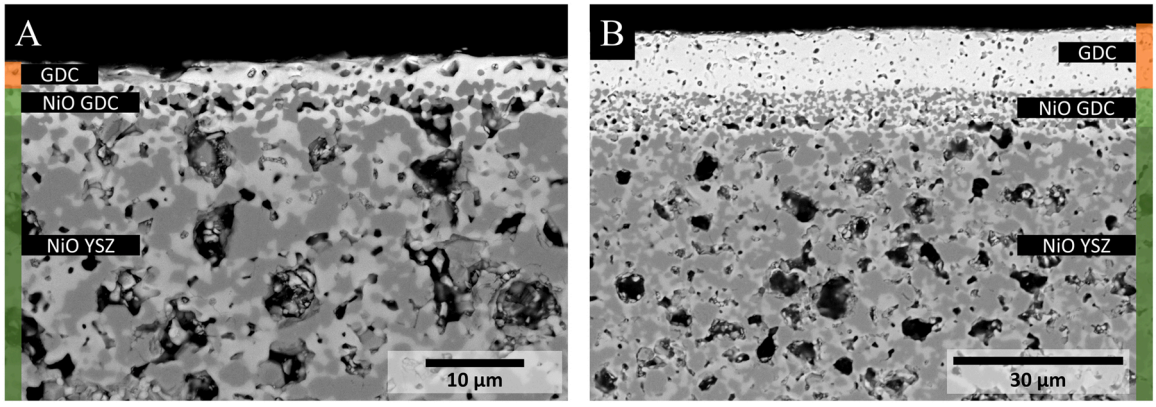

Fig. 16. Scanning electron micrographs of half-cells taken with a BSE detector. GDC electrolyte layers of two different pastes were printed and sintered at 1400 °C. A: GDC paste displayed dominating viscous behavior tan $\delta >> 1$ resulting in an average layer thickness of 2.3 ± 0.5 µm. B: GDC paste showed dominating elastic behavior tan $\delta < 1$ resulting in an average layer thickness of 10.3 ± 0.2 µm.

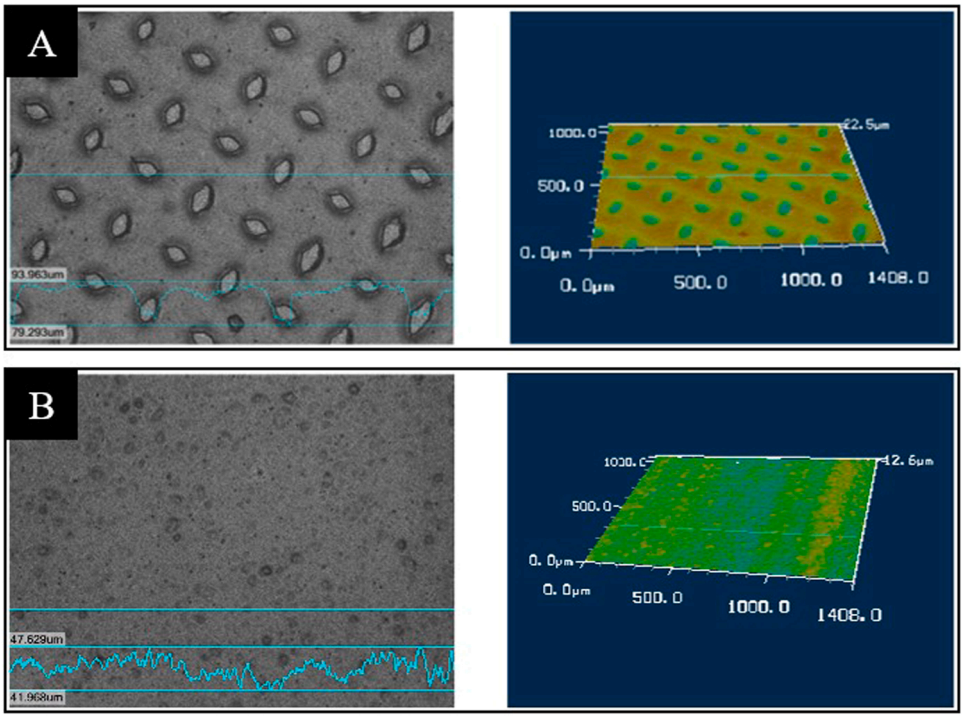

Fig. 17. Laser microscope images with depth profile scans of screen-printed GDC electrolyte surfaces on fuel electrode supports, sintered at 1400 °C. Layer in (A) shows prominent screen imprints due to a yield point at a high deformation of approx. 60 %. Layer in (B) has a yield point at lower deformations due to a lower binder-to-ceramic surface ratio and shows no screen imprints.

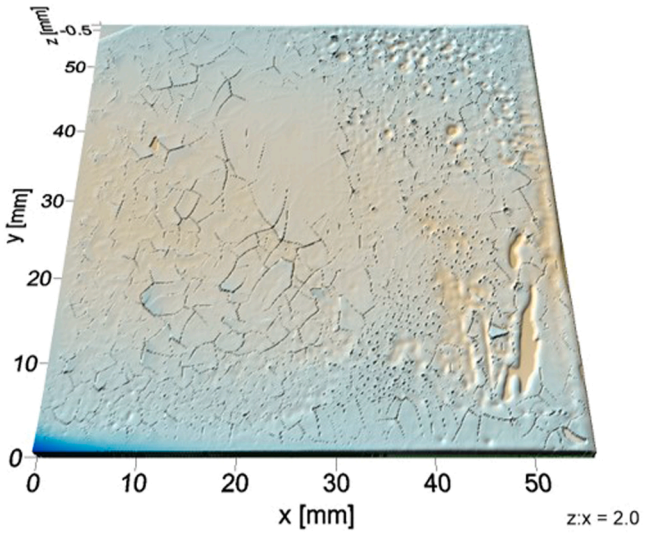

Fig. 18. Topography image taken with the optical inspection system CT200 of a dry screen-printed GDC electrolyte layer made from Paste P1. Layer shows visible drying cracks, likely resulting from too fast recovery times.

interactions shaping rheological properties. For example, it can be assumed that the influence of these components may differ in other material systems with different solvents or binder types because of different surface chemistry. Additionally, in suspensions with significantly lower solid content than that investigated here, different material interaction mechanisms may dominate, resulting in different correlations. Nevertheless, the authors expect similar trends to be observable in highly concentrated suspensions of a comparable nature. While the magnitude of the reported effects and correlations may differ in these cases, the existence of the correlations and the general trends they follow are likely to be transferable. To better understand and potentially expand upon these relationships, further rheological measurements shall be conducted in future studies. For instance, since drying behavior appears to influence the formation of cracks in dried layers, measuring rheological properties at elevated temperatures could provide insight into potential causes. Additionally, oscillatory measurements, such as amplitude sweeps at different frequencies or frequency sweeps, could provide more insight into the structural stability of the pastes. In particular, investigations in the low frequency range could provide information on the long-term stability of the pastes, while measurements at higher frequencies would allow for greater stress to be applied to the samples. In general, it is useful to investigate how significant rheological characteristics, such as yield point and damping factor, behave and shift as frequency changes. Furthermore, although it has been demonstrated that even minor changes in particle size distribution or specific surface area can significantly impact rheological properties when the paste composition remains otherwise identical, the correlations presented in this work should be verified through additional testing using a wider sample range.

CRediT authorship contribution statement

Christian Lenser: Writing – review & editing, Supervision, Project administration, Funding acquisition. **Robert Mücke:** Writing – review & editing, Methodology. **Denise J. Ramler:** Writing – original draft, Visualization, Methodology, Investigation, Formal analysis, Data curation, Conceptualization. **Norbert H. Menzler:** Writing – review & editing, Supervision, Resources. **Olivier Guillon:** Writing – review & editing, Resources.

Declaration of Generative AI and AI-assisted technologies in the writing process

During the preparation of this work the authors used DeepL Write in order to improve grammar and increase comprehensibility. After using this tool, the authors reviewed and edited the content as needed and take

full responsibility for the content of the publication.

Declaration of Competing Interest

The authors declare that they have no known competing financial interests or personal relationships that could have appeared to influence the work reported in this paper.

Acknowledgements

The authors gratefully acknowledge the funding by the German Federal Ministry of Education and Research (BMBF) for the ElChFest project (Elektro-chemo-mechanische Modellierung von Ceroxid-basierten Festoxidelektrolysezellen), [grant number 03SF0641A]. Open access publication fees are covered by the German Research Foundation (DFG).

Appendix A. Supporting information

Supplementary data associated with this article can be found in the online version at doi:10.1016/j.jeurceramsoc.2025.117570.

References

[1] A. Hauch, S.D. Ebbesen, S.H. Jensen, M. Mogensen, Highly efficient high temperature electrolysis, J. Mater. Chem. 18 (20) (2008) 2331, https://doi.org/10.1039/b718822f.
[2] M. Cassidy, Trends in the processing and manufacture of solid oxide fuel cells, WIREs Energy Environ. 6 (5) (2017) e248, https://doi.org/10.1002/wene.248.
[3] S. Häfele, M. Hauck, J. Dailly, Life cycle assessment of the manufacture and operation of solid oxide electrolyser components and stacks, Int. J. Hydrog. Energy 41 (31) (2016) 13786–13796, https://doi.org/10.1016/j.ijhydene.2016.05.069.
[4] N.H. Menzler, F. Tietz, S. Uhlenbruck, H.P. Buchkremer, D. Stöver, Materials and manufacturing technologies for solid oxide fuel cells, J. Mater. Sci. 45 (12) (2010) 3109–3135, https://doi.org/10.1007/s10853-010-4279-9.
[5] C. Bischof, et al., Microstructure optimization of nickel/gadolinium-doped ceria anodes as key to significantly increasing power density of metal-supported solid oxide fuel cells, Int. J. Hydrog. Energy 44 (59) (2019) 31475–31487, https://doi.org/10.1016/j.ijhydene.2019.10.010.
[6] W.J. Bowman, J. Zhu, R. Sharma, P.A. Crozier, Electrical conductivity and grain boundary composition of Gd-doped and Gd/Pr co-doped ceria, Solid State Ion. 272 (2015) 9–17, https://doi.org/10.1016/j.ssi.2014.12.006.
[7] K. Eguchi, T. Setoguchi, T. Inoue, H. Arai, Electrical properties of ceria-based oxides and their application to solid oxide fuel cells, Solid State Ion. 52 (1–3) (1992) 165–172, https://doi.org/10.1016/0167-2738(92)90102-U.
[8] V.V. Kharton et al., Ceria-based materials for solid oxide fuel cells.
[9] A. Schwiers, C. Lenser, O. Guillon, N.H. Menzler, Interdiffusion at electrochemical interfaces between yttria-stabilized zirconia and doped ceria, J. Eur. Ceram. Soc. 43 (14) (2023) 6189–6199, https://doi.org/10.1016/j.jeurceramsoc.2023.06.015.
[10] H. Xu, K. Cheng, M. Chen, L. Zhang, K. Brodersen, Y. Du, Interdiffusion between gadolinia doped ceria and yttria stabilized zirconia in solid oxide fuel cells: experimental investigation and kinetic modeling, J. Power Sources 441 (2019) 227152, https://doi.org/10.1016/j.jpowsour.2019.227152.
[11] M.R. Somalu, A. Muchtar, W.R.W. Daud, N.P. Brandon, Screen-printing inks for the fabrication of solid oxide fuel cell films: a review, Renew. Sustain. Energy Rev. 75 (2017) 426–439, https://doi.org/10.1016/j.rser.2016.11.008.
[12] M.R. Somalu, V. Yufit, N.P. Brandon, The effect of solids loading on the screen-printing and properties of nickel/scandia-stabilized-zirconia anodes for solid oxide fuel cells, Int. J. Hydrog. Energy 38 (22) (2013) 9500–9510, https://doi.org/10.1016/j.ijhydene.2012.06.061.
[13] R. Mücke, O. Büchler, N.H. Menzler, B. Lindl, R. Vaßen, H.P. Buchkremer, High-precision green densities of thick films and their correlation with powder, ink, and film properties, J. Eur. Ceram. Soc. 34 (15) (2014) 3897–3916, https://doi.org/10.1016/j.jeurceramsoc.2014.04.012.
[14] P. Ried, et al., Processing of YSZ screen printing pastes and the characterization of the electrolyte layers for anode supported SOFC, J. Eur. Ceram. Soc. 28 (9) (2008) 1801–1808, https://doi.org/10.1016/j.jeurceramsoc.2007.11.018.
[15] P. Von Dollen, S. Barnett, A study of screen printed yttria-stabilized zirconia layers for solid oxide fuel cells, J. Am. Ceram. Soc. 88 (12) (2005) 3361–3368, https://doi.org/10.1111/j.1551-2916.2005.00625.x.
[16] D. Marani, C. Gadea, J. Hjelm, P. Hjalmarsson, M. Wandel, R. Kiebach, Influence of hydroxyl content of binders on rheological properties of cerium–gadolinium oxide (CGO) screen printing inks, J. Eur. Ceram. Soc. 35 (5) (2015) 1495–1504, https://doi.org/10.1016/j.jeurceramsoc.2014.11.025.
[17] C.P. Hsu, R.H. Guo, C.C. Hua, C.-L. Shih, W.-T. Chen, T.-I. Chang, Effect of polymer binders in screen printing technique of silver pastes, J. Polym. Res 20 (10) (2013) 277, https://doi.org/10.1007/s10965-013-0277-3.
[18] M.R. Somalu, V. Yufit, I.P. Shapiro, P. Xiao, N.P. Brandon, The impact of ink rheology on the properties of screen-printed solid oxide fuel cell anodes, Int. J. Hydrog. Energy 38 (16) (2013) 6789–6801, https://doi.org/10.1016/j.ijhydene.2013.03.108.
[19] S. Murakami, et al., Effects of ethyl cellulose polymers on rheological properties of (La,Sr)(Ti,Fe)O3-terpineol pastes for screen printing, Ceram. Int. 40 (1) (2014) 1661–1666, https://doi.org/10.1016/j.ceramint.2013.07.057.
[20] M.R. Somalu, A. Muchtar, N.P. Brandon, Understanding the rheology of screen-printing inks for the fabrication of SOFC thick films, ECS Trans. 68 (1) (2015) 1323–1331, https://doi.org/10.1149/06801.1323ecst.
[21] M.R. Somalu, N.P. Brandon, Rheological studies of nickel/scandia-stabilized-zirconia screen printing inks for solid oxide fuel cell anode fabrication, J. Am. Ceram. Soc. 95 (4) (2012) 1220–1228, https://doi.org/10.1111/j.1551-2916.2011.05014.x.
[22] Y. Zhang, et al., A study of the process parameters for yttria-stabilized zirconia electrolyte films prepared by screen-printing, J. Power Sources 160 (2) (2006) 1065–1073, https://doi.org/10.1016/j.jpowsour.2006.02.074.
[23] J.S. Reed, J.S. Reed. Principles of ceramics processing, Second ed., Wiley, New York, 1995.
[24] K. Reinhardt, N. Hofmann, M. Eberstein, The importance of shear thinning, thixotropic and viscoelastic properties of thick film pastes to predict effects on printing performance. 2017 21st European Microelectronics and Packaging Conference (EMPC) & Exhibition, Warsaw, IEEE, Poland, 2017, pp. 1–7, https://doi.org/10.23919/EMPC.2017.8346831.
[25] T.G. Mezger. Das Rheologie Handbuch, Fifth ed., Vincentz, Hannover, 2016.
[26] P. Wei, C. Cipriani, C.-M. Hsieh, K. Kamani, S. Rogers, E. Pentzer, Go with the flow: rheological requirements for direct ink write printability, J. Appl. Phys. 134 (10) (2023) 100701, https://doi.org/10.1063/5.0155896.
[27] Malvern Instruments Limited, Understanding Yield Stress Measurements, White Paper, Worcestershire, UK, 2015.
[28] N. Tarbă, M.-L. Voncilă, C.-A. Boiangiu, On generalizing sarle's bimodality coefficient as a path towards a newly composite bimodality coefficient, Mathematics 10 (7) (2022) 1042, https://doi.org/10.3390/math10071042.
[29] R. Moreno, Better ceramics through colloid chemistry, J. Eur. Ceram. Soc. 40 (3) (2020) 559–587, https://doi.org/10.1016/j.jeurceramsoc.2019.10.014.
[30] L. Xing-Bang, Z. He, Z. Jing-Xian, D. Yu-Sen, J. Dong-Liang, Effect of powder characteristics on the rheological performance of resin-based zirconia suspension for stereolithography, J. Inorg. Mater. (2019) 13, https://doi.org/10.15541/jim20190091.
[31] D.E. Riemer, The theoretical fundamentals of the screen printing process, Microelectron. Int. 6 (1) (1989) 8–17, https://doi.org/10.1108/eb044350.
[32] G.J. Donley, W.W. Hyde, S.A. Rogers, F. Nettesheim, Yielding and recovery of conductive pastes for screen printing, Rheol. Acta 58 (6–7) (2019) 361–382, https://doi.org/10.1007/s00397-019-01148-w.
[33] T.K. Goh, K.D. Coventry, A. Blencowe, G.G. Qiao, Rheology of core cross-linked star polymers, Polymer 49 (23) (2008) 5095–5104, https://doi.org/10.1016/j.polymer.2008.09.030.